Computational and Structural Biotechnology Journal 20 (2022) 3019–3029

COMPUTATIONAL AND STRUCTURAL BIOTECHNOLOGY JOURNAL

journal homepage: www.elsevier.com/locate/csbj

Computational design of an apoptogenic protein that binds BCL-xL and MCL-1 simultaneously and potently

Seonghoon Kim [a], Hee-Sung Park [b], Byung-Ha Oh [a,*]

[a] Department of Biological Sciences, KAIST Institute for the Biocentury, Korea Advanced Institute of Science and Technology, Daejeon 34141, Republic of Korea
[b] Department of Chemistry, Korea Advanced Institute of Science and Technology, Daejeon 34141, Republic of Korea

ARTICLE INFO

Article history:
Received 21 April 2022
Received in revised form 9 June 2022
Accepted 9 June 2022
Available online 14 June 2022

Keywords:
Computational protein design
X-ray crystallography
Apoptosis
Cancers
Therapeutic protein

ABSTRACT

One of the hallmarks of cancer cells is their ability to evade apoptosis, which confers survival advantages and resistance to anti-cancer drugs. Cancers often exhibit overexpression of anti-apoptotic BCL-2 proteins, the loss of which triggers apoptosis. In particular, the inhibition of both BCL-xL and MCL-1, but neither one individually, synergistically enhances apoptotic cell death. Here, we report computational design to produce a protein that inhibits both BCL-xL and MCL-1 simultaneously. To a reported artificial three-helix bundle whose second helix was designed to bind MCL-1, we added a fourth helix and designed it to bind BCL-xL. After structural validation of the design and further structure-based sequence design, we produced a dual-binding protein that interacts with both BCL-xL and MCL-1 with apparent dissociation constants of 820 pM and 196 pM, respectively. Expression of this dual binder in a subset of cancer cells induced apoptotic cell death at levels significantly higher than those induced by the pro-apoptotic BIM protein. With a genetic fusion of a mitochondria-targeting sequence or the BH3 sequence of BIM, the activity of the dual binder was enhanced even further. These data suggest that targeted delivery of this dual binder alone or as a part of a modular protein to cancers in the form of protein, mRNA, or DNA may be an effective way to induce cancer cell apoptosis.

1. Introduction

The BCL-2 family of proteins regulates the mitochondria-mediated apoptotic pathway, which ultimately leads to the release of apoptogenic proteins, such as cytochrome *C* and Smac/DIABLO, from mitochondria into the cytosol via mitochondrial outer membrane permeabilization (MOMP) [1,2]. These proteins contain up to four BCL-2 homology (BH) domains, which mediate intermolecular interactions between family members. Typically, the BH3 domain of one protein interacts with an extended hydrophobic groove, known as the BH3-binding groove of another protein. BCL-2 family members are divided into three groups depending on their function and their number of BH domains: (i) pro-apoptotic and pore-forming proteins BAX, BAK, and BOK, which contain BH1 through BH3; (ii) pro-apoptotic BH3-only proteins, such as BIM, BID, BAD, PUMA, NOXA, and BNIP3; and (iii) anti-apoptotic BCL-2 proteins, such as BCL-2, BCL-B, BCL-W, BCL-xL, BFL-1 (A1), and MCL-1, all of which contain at least three or even all four BH domains [3,4]. BH3-only proteins belong to one of two subclasses: (i) activator BH3-only proteins that bind and activate BAX and BAK and that bind the anti-apoptotic BCL-2 proteins (BIM and BID) as well as (ii) sensitizer BH3-only proteins that only bind the anti-apoptotic BCL-2 proteins (BAD, PUMA, etc.).

The three groups of BCL-2 family proteins control MOMP in response to developmental or stress signals by directly binding to one another. When the activator BH3-only proteins bind the BH3-binding groove of BAX and BAK, a series of conformation changes occur, leading to the homo-oligomerization of BAX/BAK. This induces the formation of a protein-conducting pore on the MOM, which then irreversibly triggers cell death [5–7]. This engagement between these two groups of pro-apoptotic BCL-2 proteins is inhibited by the anti-apoptotic BCL-2 proteins, which sequester both BAX/BAK and the activator BH3-only proteins also through the interaction between the BH3 domain and BH3-binding groove [4]. Ultimately, whether a cell remains alive or commits apoptosis is determined by the balance between pro-apoptotic and anti-apoptotic engagements, and this is mainly affected by the relative abundance and binding affinity of the various BCL-2 family protein members in the MOM [4,8,9].

Many cancer cells evade apoptosis and achieve sustained cell growth by overexpressing anti-apoptotic BCL-2 proteins [10–13].

* Corresponding author.
E-mail address: bhoh@kaist.ac.kr (B.-H. Oh).

https://doi.org/10.1016/j.csbj.2022.06.021

Their survival often depends on not just one, but many anti-apoptotic BCL-2 proteins. This is supported by expression profiling of MCL-1, BCL-2, and BCL-xL in multiple myeloma cells [14,15] and by small interference RNA experiments in which the silencing of two genes, *MCL-1* and *BCL-xL*, but not either one individually, induced apoptosis in many cancer cells [16,17]. BCL-xL, MCL-1, and BCL-2 appear to be the three most frequently overexpressed anti-apoptotic BCL-2 proteins in cancer cells [15,18–20], but their expression is complex and varies depending on cancer type and even within a single cancer type [14,15,20].

Hydrocarbon stapled-BH3 peptides that can cross the cell membrane induce apoptosis in human leukemia cells [21]. These peptides work by displacing pro-apoptotic BCL-2 family members from anti-apoptotic family members [22] or by directly binding and activating BAX [23]. A variety of small molecules that mimic BH3 have been developed that can interfere with anti-apoptotic BCL-2 proteins. These include ABT-199 (Venetoclax), which is specific for BCL-2; A-1155463, which is specific for BCL-2; ABT-263 (navitoclax), which is specific for both BCL-2 and BCL-xL; S63845, which is specific for MCL-1 [18]; and obatoclax, which is a pan-BCL-2 inhibitor [18,24]. Venetoclax is approved by the US Food and Drug Administration for the treatment of chemotherapy-refractory chronic lymphocytic leukemia, which depends on BCL-2 for sustained cell growth [25,26].

In principle, an unstable bioactive peptide can be converted into a stable protein form. The unstable BH3 peptide was engrafted into a set of very stable *de novo* designed proteins which bind to a single anti-apoptotic BCL-2 protein with high potency and specificity [27,28]. These designed proteins induced apoptotic cell death of lymphocytes infected with Epstein-Barr virus which encodes anti-apoptotic BCL-2 homolog, or induced apoptotic death of colorectal cancer cells in combination with the small molecules inhibiting each anti-apoptotic BCL-2 protein upon intracellular expression.

We computationally designed a four-helix bundle protein that simultaneously binds both MCL-1 and BCL-xL with potent affinities. We found that this protein effectively induces the apoptosis of cancer cells that express these anti-apoptotic proteins, and this apoptogenic activity was even further enhanced upon fusion of the BH3 or mitochondria-targeting sequence of BIM to the designed protein.

2. Materials and methods

2.1. Computational design

The Rosetta software was used for computational protein design [29]. The BundleGridSampler mover was used to generate a set of fourth helices to add to αMCL1 [30]. Then, the models were visually inspected and interface designs were produced for the area within 6 Å of the surfaces of αMCL1 and each fourth helix. One of the resulting two hundred design models was selected based on total energy score, ΔΔG, interface shape complementarity, and a visual inspection. The Remodel mover was used to link the fourth helix to the C-terminus of αMCL1 [31], and the FastDesign mover was used for the sequence design of the fourth helix and its interface with αMCL1 [32,33]. The crystal structure of BCL-xL in complex with BIM BH3 peptide (PDB entry: 3FLD) [34] was used for motif grafting the BH3 sequence onto the fourth helix with seven residues designated as hotspot residues. Apart from these hotspot residues, all residues of the four-helix bundle within 8.3 Å of BCL-xL were subjected to sequence design. Eight of the five hundred resulting design models were selected based on total energy score, ΔΔG, interface shape complementarity, and a visual inspection. In the second round of the design, the crystal structure of 4H_αBM_1 in complex with BCL-xL was used for sequence optimization, with only six residues allowed to change.

2.2. Protein expression, purification, and size-exclusion chromatography

DNA fragments encoding the designed proteins were synthesized (IDT) and cloned into pJK hTx or pCW57.1 vectors for protein expression in *E.coli* or mammalian cells, respectively. BCL-2 family proteins were also expressed from the pJK hTx vector. The BCL-2 protein constructs were BCL-2 (1–34:chimeric loop:92–203), BCL-B (1–177;C30S/C138S), BCL-W (1–164), BCL-xL (1–44:85–209), BFL-1 (1–151;C4S/C19S), MCL-1 (172–321). For biotinylation of the BCL-2 proteins, BirA was expressed from the pCDFduet vector with BCL-2 proteins that included a C-terminal biotinylation sequence (GLNDIFEAQKIEWHE). Proteins were expressed at 18 °C in the *E.coli* Lemo(DE3) strain, grown in TB medium. Cells were collected by centrifugation, resuspended, and lysed by sonication. Supernatants were loaded onto pre-equilibrated Co-NTA resin (Thermo Fisher Scientific), and bound proteins were eluted with a buffer solution containing 100 mM NaCl, 20 mM Tris (pH 7.5), and 150 mM imidazole. The eluted proteins were further purified by size-exclusion chromatography using a HiLoad 26/60 Superdex 75 column (GE Healthcare). For a qualitative binding assay, purified proteins were loaded onto a Superdex 75 Increase 10/300 GL column (GE Healthcare) and the apparent mass of the protein complexes was estimated based on the elution of size marker proteins.

2.3. Crystallization and structure determination

4H_αBM_1 or 4H_αBM_2 was mixed with BCL-xL and the resulting complexes were isolated by size-exclusion chromatography using a HiLoad 26/60 Superdex 75 column (GE Healthcare). 4H_αBM_2 bound to MCL-1 was purified using the same method. Crystals were obtained by the hanging-drop vapor diffusion method at 20 °C. Crystals of 4H_αBM_1–BCL-xL were obtained by mixing the complex (52.3 mg/ml) with a precipitant solution containing 4% PEG 3,000 (w/v) and 0.1 M sodium acetate (pH 4.5). Crystals of 4H_αBM_2–BCL-xL were obtained by mixing the complex (55 mg/ml) with a precipitant solution containing 10% PEG 10,000 (w/v) and 0.1 M sodium acetate (pH 4.5). Crystals of 4H_αBM_2–MCL-1 were obtained by mixing the complex (23.5 mg/ml) with precipitant solution containing 12% PEG 6,000 (w/v), 0.1 M magnesium chloride, and 0.1 M ADA (pH 6.5). The crystals were immersed briefly in a cryoprotectant solution, which was the same as the reservoir solution with an additional 17.5% ethylene glycol for the 4H_αBM_1–BCL-xL and 4H_αBM_2–MCL-1 crystals or 17% glycerol for the 4H_αBM_2–BCL-xL crystals. X-ray diffraction datasets were collected on beamline 5C at Pohang Accelerator Laboratory, South Korea. The structure of the 4H_αBM_1–BCL-xL complex was determined via the single anomalous dispersion method. Then, automatic model building into the electron densities and structure refinement were performed using the PHENIX software suit [35]. The structures of the 4H_αBM_2–BCL-xL and the 4H_αBM_2–MCL-1 complexes were determined via molecular replacement using their respective design models as search models, followed by structure refinement using PHENIX [36]. Iterative rounds of manual model building and refinement were carried out using the programs COOT [37] and PHENIX. All structures were illustrated using the PYMOL software [38]. Crystallographic data statistics are summarized in Table 1.

2.4. Surface plasmon resonance (SPR)

SPR data were collected on an 8 K device (GE Healthcare). A Series S Biotin CAPture kit (GE Healthcare) was used to immobilize

Table 1
X-ray data collection and structure refinement statistics.

Data collection	4H_αBM_1–BCL-xL	4H_αBM_2–BCL-xL	4H_αBM_2–MCL-1
X-ray source[a]	BL5C, PAL	BL5C, PAL	BL5C, PAL
Space group	P1	P1	P1
Unit cell dimensions			
a, b, c (Å)	60.61,68.54,80.52	60.93,69.05,79.99	67.99,74.77,92.16
α, β, γ (°)	100.89,110.57,108.73	100.79,110.00,108.67	70.83,89.59,67.58
Wavelength (Å)	0.97403	0.97959	0.97959
Resolution (Å)	50.0–1.9 (1.93–1.90)	29.21–1.9 (1.97–1.90)	29.46–2.38 (2.47–2.38)
R_{sym} (%)	8.7 (32.2)[b]	6.6 (79.1)[b]	4.8 (63.6)
$I/\sigma(I)$	21.8 (2.8)	10.8 (1.3)	14.0 (1.8)
Completeness (%)	96.7 (95.3)	96.68 (95.81)	97.36 (96.94)
Redundancy	3.6 (3.1)	3.7 (3.48)	3.6 (3.64)
Refinement			
Resolution (Å)	38.1–1.9	29.21–1.9	29.46–2.38
No. of reflections	162,019	83,334	61,287
R_{work}/R_{free} (%)	16.57/19.67	17.15/20.61	20.24/24.03
R.m.s deviations			
bond length (Å)/angle (°)	0.016/1.66	0.007/0.781	0.006/1.009
Average B-values ($Å^2$)	32.94	41.36	70.89
Ramachandran plot (%)			
Favored	98.1	98.1	98.4
Allowed	1.9	1.9	1.6

[a] Beamline 5C at Pohang Accelerator Laboratory.
[b] The numbers in parentheses are the statistics from the highest resolution shell.

biotinylated anti-apoptotic BCL-2 proteins, and all experiments were conducted in HBS-EP + buffer solution (10 mM HEPES, 150 mM NaCl, 3 mM EDTA, 0.005% Surfactant P20; GE Healthcare). Biotinylated anti-apoptotic BCL-2 proteins were immobilized on the CAP chip until the response units reached 100. Serially diluted analytes were injected at a flow rate of 30 μl/min. Analytes were used at 20 nM for single concentration experiments. Dissociation constants (K_D) and kinetic parameters (k_a and k_d) were estimated using a 1:1 Langmuir binding model with Biacore 8 K evaluation software (GE Healthcare).

2.5. Cell culture

HEK293T, A375, MEWO, SW620, HCT-116, and K562 cell lines were maintained in DMEM supplemented with an antibiotic–antimycotic solution and 10% FBS. All cell lines were incubated at 37 °C in a humidified incubator containing 5% CO_2.

2.6. Lentivirus production and infection

The pCW57.1 lentiviral vector was used for cloning 3xFLAG-tagged proteins and for generating lentivirus. HEK293T cells grown in T25 flasks were transfected with 2.7 μg pCW57.1, 1.4 μg pRSV-REV, 1.9 μg pMD2.G, and 2.9 μg pMDL g/p RRE vectors (Addgene #41393, #12253, #12259, and #12251, respectively) using Lipofectamine 3000 (GE Healthcare) according to the manufacturer's instructions. Viral supernatants were harvested and filtered using a 0.45 μm polyethersulfone filter 72 h after transfection. Supernatants containing viruses were used immediately or stored in aliquots at −80 °C. A375, MEWO, SW620, HCT-116, and K562 cells were infected with each viral supernatant along with 8 μg/ml polybrene. Infected pools were then selected by 2 μg/ml puromycin treatment after a 48 h incubation at 37 °C. Puromycin-resistant pools were used following cell viability assays and western blot analyses with and without 2 μg/ml doxycycline.

2.7. Cell viability assay

Cell viability was determined using the WST-1 reagent (Roche) according to the manufacturer's instructions. Successfully transduced cell lines were seeded on 96-well plates at 5000 cells per well in 100 μl culture medium. After a 24 h incubation, 2 μg/ml doxycycline was added to the culture medium to induce protein expression. A 100-fold lower doxycycline concentration was used for BIM expression. WST-1 reagent was added after a 12 h incubation, and absorbance was measured at 450 nm and 690 nm using a Spark 10 M microplate reader (Tecan).

2.8. Western blot analysis

Cells were harvested 12 h after doxycycline treatment and lysed in RIPA buffer (Thermo Fisher Scientific) supplemented with a protease inhibitor cocktail (Quartett) and a phosphatase inhibitor cocktail (Sigma). For BIM detection, the pan-caspase inhibitor Z-VAD-FMK (MedChemExpress) was added 30 min prior to the addition of doxycycline. The cell lysates were then incubated for 1 h on ice and centrifuged at 15,000*g* for 30 min at 4 °C. Total protein concentrations for the whole-cell lysates were measured using a BCA protein assay kit (Thermo Fisher Scientific). Equal amounts of the lysates were resolved on SDS-PAGE gels and transferred to PVDF membranes. These were then incubated with primary antibody overnight at 4 °C before being washed three times with TBS-T buffer and incubated with a secondary antibody for 1 h at room temperature. Chemiluminescence was generated with ECL Western Blotting Substrate (Thermo Fisher Scientific) and detected using a ChemiDoc MP (Bio-Rad). All images were analyzed using Image Lab (Bio-Rad). The antibodies used for the western blots were: anti-FLAG (Sigma, F1804), anti-BCL-xL (Abcam, ab32370), anti-MCL-1 (Abcam, ab32087), anti-γ-H2A.X (Abcam, ab81299), anti-PARP (Abcam, 191217), anti-β-actin (Abcam, ab6276), HRP-conjugated anti-rabbit IgG (Abcam, ab205718), and HRP-conjugated anti-mouse IgG (Abcam, ab6728).

3. Results

3.1. Computational design of a BCL-xL/MCL-1 binding protein

We began with a *de novo* designed three-helix bundle structure, called αMCL1, which binds tightly and specifically to MCL-1 with a dissociation constant (K_D) of 150 pM [28]. This protein has a BH3-like motif in its second helix that is responsible for its interaction with MCL-1. In addition to this primary site of intermolecular interaction, the other two helices also contribute to MCL-1 binding, improving its specificity. This is clear in the αMCL1–MCL-1 co-crystal structure (PDB entry: 5JSB) [28]. We speculated that αMCL1 could be converted into a four-helix bundle by adding an extra α-helix, and this fourth α-helix could be designed to bind BCL-xL without affecting MCL-1 binding at the opposite side. Using parametric α-helix building, loop modeling, and interface sequence design with the Rosetta software suite [29], we generated a total of 200 four-helix bundles (Fig. 1A). Based on the Rosetta all-atom energy values and visual inspection, we selected one of the output models for further experiments. We then used this final four-helix bundle (designated 4H_αMCL1) as a template upon which to engraft the crystal structure of BCL-xL bound to the BIM BH3 peptide [34]. Onto the fourth helix, we used the motif grafting protocol in Rosetta with the "hotspot" option to maintain the seven highly conserved BH3 residues of BIM (i.e., Ile148, Ala149, Leu152, Ile155, Gly156, Asp157, and Phe159) [39]. Next, we subjected the resulting output models to further sequence design in which any residues within 8.3 Å from BCL-xL (apart from the hotspot residues) were allowed to change and those within 8.3–10 Å from BCL-xL were restricted to repacking. A total of 500 models were then evaluated according to the following filtering criteria: Rosetta all-atom energy < -660, interface shape complementarity > 0.62, and buried unsatisfied polar atoms $\leq$ 3 (Fig. 1B). Considering the high success rate of motif grafting in general, we selected only the eight best designs after visual inspection. We then cloned and produced all eight in *E. coli* for experimental validation.

3.2. Biochemical and structural validation of the BCL-xL/MCL-1 binders

Among the eight designs we selected for further experiments, five were highly soluble and we were able to purify them to homogeneity. Using surface plasmon resonance (SPR), we evaluated their binding to BCL-xL and selected one with which to proceed (Fig. 2A). By performing SPR runs with different concentrations of

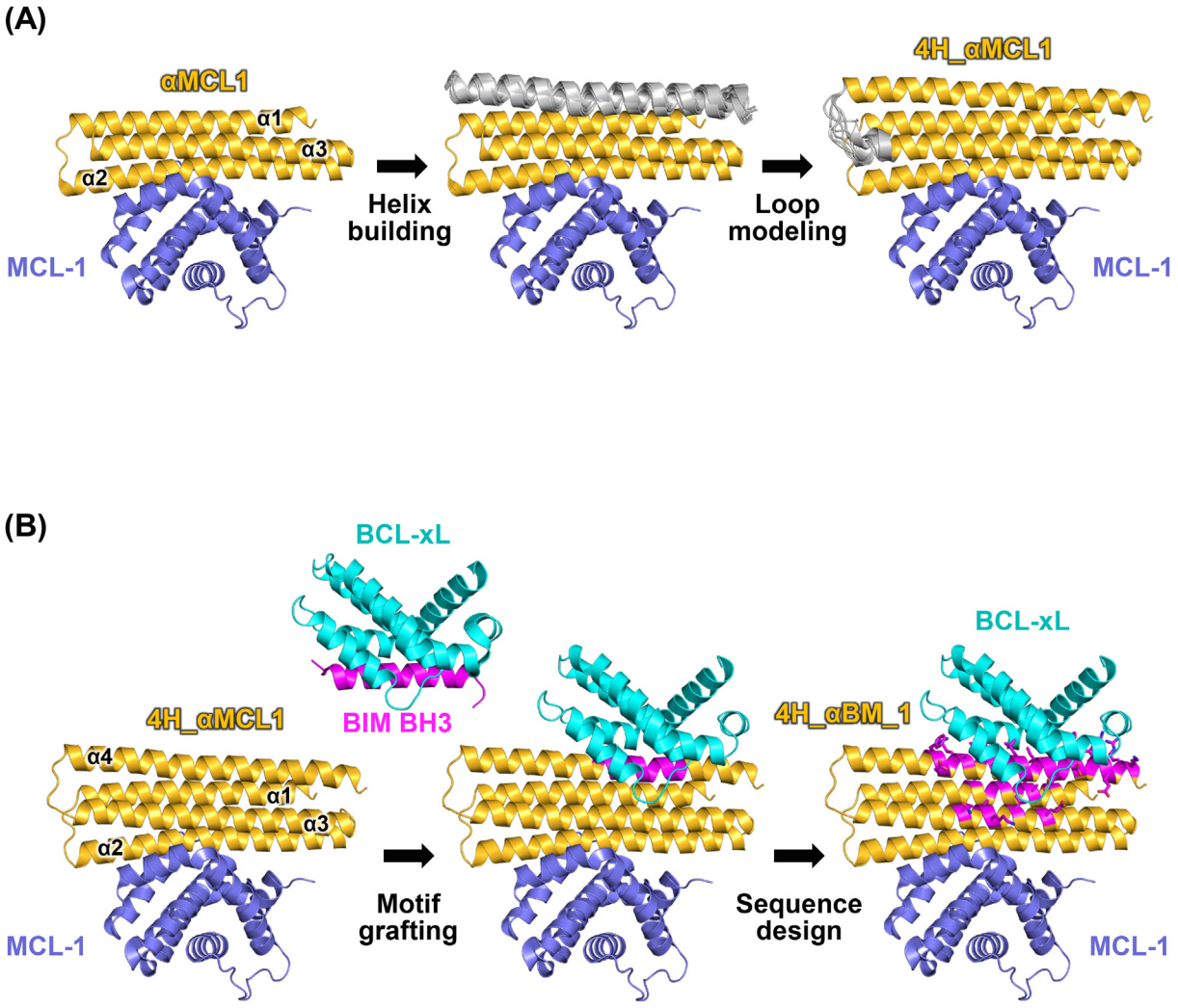

Fig. 1. Computational design of BCL-xL/MCL-1 binders. (A) The computational design procedure used to generate 4H_αMCL1. The crystal structure of αMCL1 in complex with MCL-1 (PDB entry: 5JSB) was used as the input scaffold. Parametric generation of the fourth α-helix and interface design between it and αMCL1 was performed. Next, blueprint-based loop modeling was performed to connect the two together. (B) Motif grafting and sequence design. The BIM BH3 sequence in the BCL-xL–BIM BH3 structure (PDB entry: 3FDL) was grafted onto the fourth α-helix of 4H_αMCL1, followed by a sequence design of the interface.

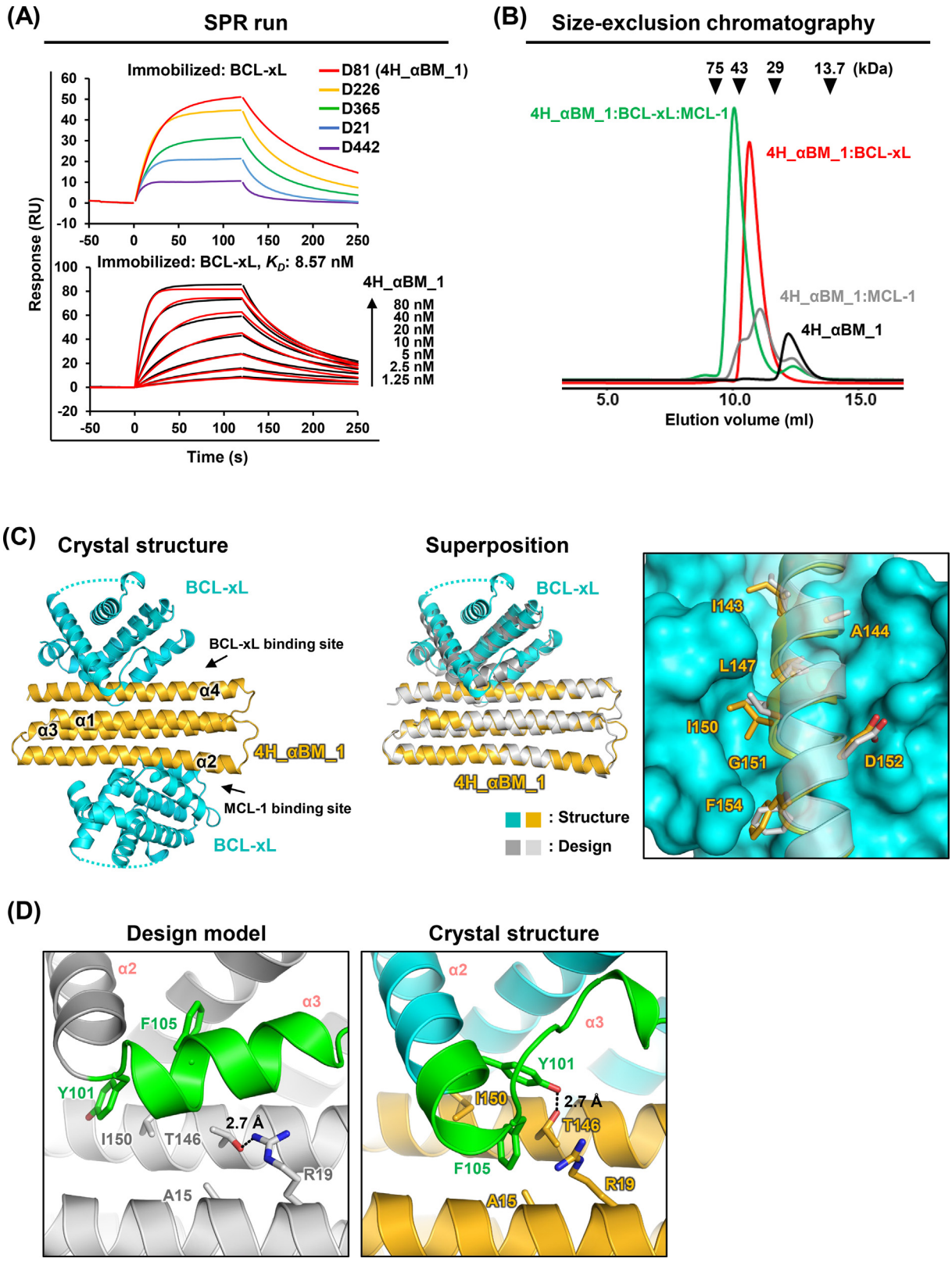

Fig. 2. Experimental validation. (A) Screening, selection, and K_D measurement by SPR. (*Top*) The five indicated designs were tested for binding to BCL-xL (immobilized on a biosensor chip). (*Bottom*) The K_D of the design that exhibited the highest binding signal (4H_αBM_1) was determined by performing SPR at the indicated concentrations. Raw data (black lines) were fitted (red lines). (B) Size-exclusion chromatography. 1:1 mixtures of both 4H_αBM_1:BCL-xL and 4H_αBM_1:MCL-1 were eluted as if they were a 1:1 heterodimer. A 1:1:1 mixture of 4H_αBM_1:BCL-xL:MCL-1 was eluted as a heterotrimer with a 1:1:1 binding stoichiometry. The black arrows indicate the elution positions of the standard size markers. (C) Crystal structure of 4H_αBM_1–BCL-xL. (*Left*) BCL-xL binds both sides of 4H_αBM_1. (*Middle*) Superposition of 4H_αBM_1–BCL-xL and the design model. The RMSD for the aligned Cα atoms is 1.062 Å. (*Right*) Magnified views show the preserved hotspot residues in the binding interface: Ile143, Ala144, Leu147, Ile150, Gly151, Asp152, and Phe154. (D) Conformational change. α3 is partially unwound and α2 is elongated in the crystal structure compared to the designed model. (For interpretation of the references to colour in this figure legend, the reader is referred to the web version of this article.)

our selected design, we measured its dissociation constant (K_D) to be 8.57 nM (Fig. 2A). Using size-exclusion chromatography, we found this protein can bind MCL-1 alone, as well as both BCL-xL and MCL-1 simultaneously. This indicates that the MCL-1 binding site is intact and that BCL-xL and MCL-1 can bind simultaneously without steric hindrance (Fig. 2B). Thus, we designated this BCL-xL/MCL-1 binding protein 4H_αBM_1.

Next, we determined the crystal structure of 4H_αBM_1–BCL-xL (Table 1). Since αMCL1 has a low affinity for BCL-xL (K_D of 340 μM) [28], we expected 4H_αBM_1 and BCL-xL to form a 1:1 complex. In the crystal structure, however, BCL-xL binds both the MCL-1 binding site and the designed BCL-xL binding site. This is likely either because of the high concentration of protein used during crystallization or because crystal packing interactions promote the binding of BCL-xL to the MCL-1 binding site. The structure we determined is closely superposable onto the designed model with a Cα root mean square deviation (RMSD) of 1.062 Å, confirming that the 4H_αBM_1 design was largely correct (Fig. 2C). We were surprised to see in the model a conformational change in BCL-xL helices α2 and α3. In comparison with the original conformation, we observed a one-turn extension of helix α2 and a loosened helical propensity of helix α3 (Fig. 2D). This conformational change is likely due to the formation of a more favorable interaction with 4H_αBM_1 because the altered BCL-xL segment is not involved in any major crystal packing interactions. Similar conformations are found in other crystal structures of BCL-xL bound to BH3 peptides [40], suggesting that this segment of BCL-xL adopts one of two alternative conformations in a context-dependent manner.

3.3. Further computational design based on the crystal structure of 4H_αBM_1–BCL-xL

If the altered conformation is more energetically favorable for binding to 4H_αBM_1, then the conformational change we observed invalidates our amino acid sampling near BCL-xL helices α2 and α3 in the sequence design step. Using the crystal structure as the template, we tried to optimize local interactions with α2 and α3 by sequence design of six selected residues that fall within 8 Å of the two helices: Asp12, Ala15, Asn16, Arg19, Ala142, and Thr146 (Fig. 3A). We then selected three of 50 resulting models using the same criteria previously described and estimated their binding affinity for BCL-xL. Compared to 4H_αBM_1, all three designs exhibited enhanced binding affinity in the SPR analysis at a single analyte concentration (Fig. 3B). The best model, which we designated 4H_αBM_2, gave an estimated K_D for binding to BCL-xL of 0.21 nM, which represents 40-fold stronger binding than 4H_αBM_1 (K_D of 8.57 nM).

Next, we determined the crystal structure of 4H_αBM_2 in complex with BCL-xL (Table 1). Again, the crystal structure indicated a 1:2 complex between 4H_αBM_2 and BCL-xL, closely matching the design model in all regions, including BCL-xL helices α2 and α3 (Fig. 3C). The structure shows that the D12I, N16R, and T146R substitutions improved intermolecular interactions. Ile12 forms hydrophobic interactions with Ala104 and Phe105 of BCL-xL, while Arg16 forms electrostatic interactions with the backbone oxygen of Ala104 at the end of BCL-xL helix α2. Especially, Arg146 of 4H_αBM_2 contributes not only electrostatic interactions but also hydrophobic interactions with its aliphatic portion; its amino group makes a hydrogen bond with Gln111 of BCL-xL, and its β, γ, and δ carbon atoms are in close contact with Phe105 of BCL-xL (Fig. 3C).

In the crystal structure, 4H_αBM_2 buries 1511 Å^2 of the solvent-accessible surface of BCL-xL, an area significantly wider than the 1160 Å^2 of BCL-xL surface buried by the BH3 peptide in the template structure used for our design (PDB entry: 3FDL). This wider coverage seems to be due to the extra interactions provided by the first and third helices of 4H_αBM_2 as well as the main interaction between the BH3-like motif on the fourth helix and BCL-xL (Fig. 3D). These extra interactions may also explain why the binding affinity of 4H_αBM_2 for BCL-xL (K_D of 0.21 nM) is much higher than the binding affinity of a 36-mer BIM BH3 peptide for BCL-xL (K_D of 6.67 nM) [41].

Although we did not obtain crystals for the trimeric complex between 4H_αBM_2–BCL-xL and MCL-1, we did determine the crystal structure for the 4H_αBM_2–MCL-1 complex (Fig. 3E, Table1). Unlike the 4H_αBM_2–BCL-xL complex, it revealed a 1:1 heterodimer between the two proteins. This indicates that the newly designed BCL-xL binding site has a lower affinity for MCL-1. When we performed a structural alignment of 4H_αBM_2–MCL-1 and αMCL1–MCL-1 (PDB entry: 5JSB), it appeared that our design did not affect the three-helix bundle structure of αMCL1 (Fig. 3E).

3.4. The affinity of the designed binding site for anti-apoptotic BCL-2 proteins

The MCL-1 binding site on the original αMCL1 is highly specific for MCL-1 [28] with a K_D of 0.15 nM. In contrast, its affinities for other anti-apoptotic BCL-2 proteins are much lower (K_D > 10 μM). To evaluate the specificity of the newly designed binding site on 4H_αBM_2, we first introduced I54E and G58E mutations into the MCL-1 binding site on the second α-helix (Fig. 3F). Mutations of these conserved residues generally prevent binding to anti-apoptotic BCL-2 proteins [42,43]. Thus, the resulting mutant protein, 4H_αBM_2(I54E/G58E), should only be able to interact with anti-apoptotic BCL-2 proteins via the newly designed binding site on the fourth α-helix. Unlike the MCL-1 binding site, the newly designed binding site binds MCL-1 with fairly high affinity (Fig. 3F). To enhance this binding specificity, we examined the structural superposition of MCL-1 on the 4H_αBM_2–BCL-xL complex, finding that we could change the Ile143 hotspot residue to leucine to introduce steric hindrance with MCL-1 without affecting BCL-xL binding (Fig. 4A, B). We then produced 4H_αBM_2(I143L/I54E/G58E), containing this I143L mutation, and measured its interactions with six different anti-apoptotic BCL-2 proteins (i.e., BCL-2, BCL-B, BCL-W, BCL-xL, BFL-1 (A1), and MCL-1) (Fig. 4C). Consistent with our hypothesis, 4H_αBM_2(I143L/I54E/G58E) exhibited ~7-fold reduced affinity for MCL-1 (K_D of 133 nM) while maintaining picomolar affinity for BCL-xL (Fig. 4C). This variant showed fairly high affinity for BCL-2 (K_D of 2.04 nM) and BCL-W (K_D of 1.59 nM), reflecting the high sequence homology of the two proteins with BCL-xL. However, it exhibited much lower affinity for BCL-B (K_D of 146 nM) and BFL-1 (K_D of 16.4 nM). This specificity-enhanced design 4H_αBM_2(I143L) was named 4H_αBM_3. We introduced L147E and G151E mutations to 4H_αBM_3 to prevent MCL-1 from binding to the BCL-xL binding site, and asked whether the original MCL-1 binding site retains the same potency. This mutant, 4H_αBM_3(L147E/G151E), tightly bound MCL-1 (K_D of 196 pM), which is similar to the affinity of αMCL1 (K_D of 150 pM) [28].

3.5. Proapoptotic activity of 4H_αBM_3

We next evaluated the apoptogenic activity of 4H_αBM_3 by using a lentivirus to induce its expression in the K562, HCT-116, SW620, MEWO, and A375 cancer cell lines, which all depend on BCL-xL and MCL-1 for growth [13,44,45]. In addition to 4H_αBM_3, we generated the 4H_αBM_3_BH3 and 4H_αBM_3_CTS constructs, in which the BIM BH3 sequence or the C-terminal sequence (CTS) of BIM, respectively, are fused to the C-terminus of 4H_αBM_3. BIM BH3 directly activates BAX/BAK. The CTS of BIM is a mitochondria-targeting sequence

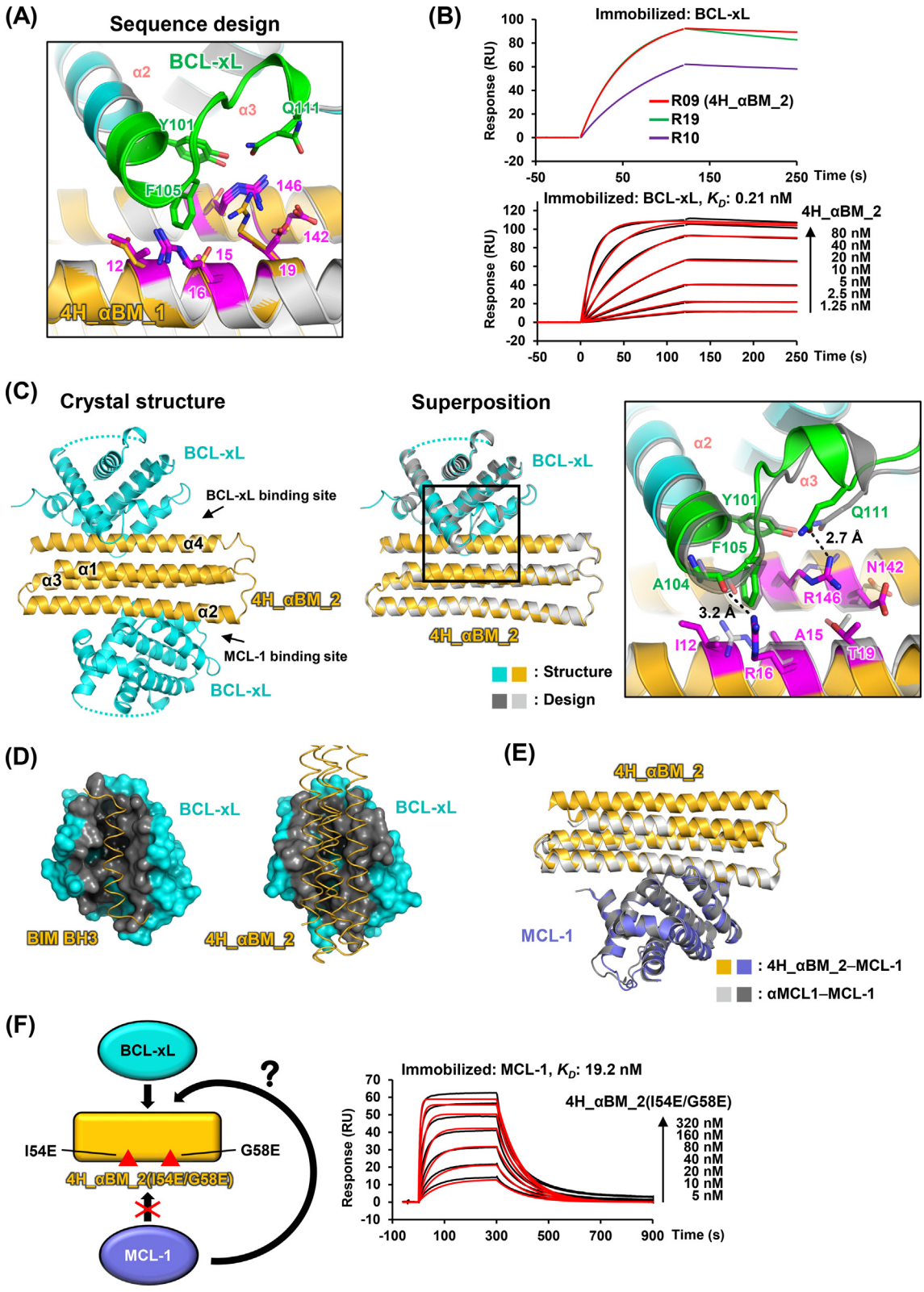

Fig. 3. Local sequence design and experimental validation. (A) Computational sequence design. The six residues shown in stick form (yellow) in the structure of 4H_αBM_1–BCL-xL (template) were chosen for sequence design to optimize their binding interaction with the α2-loop-α3 segment (green). After sequence design, three design models were selected and superposed on the crystal structure. The side chains of the six residues are indicated in magenta. (B) SPR runs. BCL-xL was immobilized on a biosensor chip and binding affinity was measured at a single concentration (20 nM) of each design (*Top*) or at the indicated concentrations of 4H_αBM_2 (*Bottom*). (C) Crystal structure of 4H_αBM_2–BCL-xL. (*Left*) A 1:2 complex between 4H_αBM_2 and BCL-xL. (*Middle*) The crystal structure is superposable on the design model (gray) with an RMSD of 0.409 Å for the aligned Cα atoms. (*Right*) Magnified view of the interactions between the α2-loop-α3 segment of BCL-xL and 4H_αBM_2. (D) The interface between BCL-xL and BIM BH3 peptide or 4H_αBM_2. BIM BH3 peptide and 4H_αBM_2 are shown as yellow wires, and the residues of BCL-xL that comprise the interface are shown in gray. (E) Crystal structure of 4H_αBM_2–MCL-1 superposed upon that of αMCL1–MCL-1. The RMSD for the aligned Cα atoms is 0.984 Å. (F) MCL-1 interaction with 4H_αBM_2(I54E/G58E). (*Left*) Schematic indicating the location of mutations introduced into the MCL-1 binding site (triangles). (*Right*) SPR runs. MCL-1 was immobilized on a biosensor chip and binding affinity was measured with serially-diluted 4H_αBM_2(I54E/G58E). (For interpretation of the references to colour in this figure legend, the reader is referred to the web version of this article.)

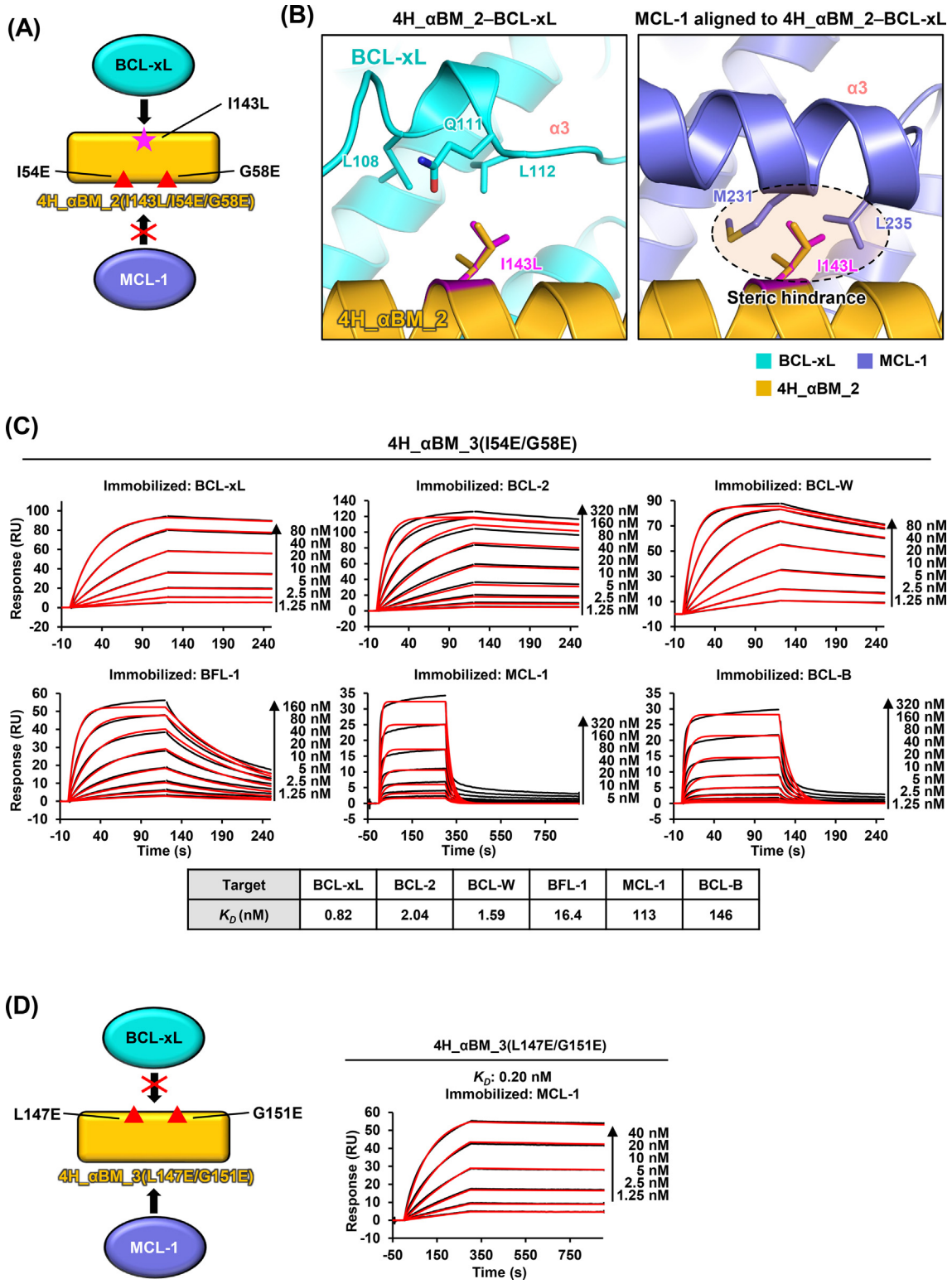

Target	BCL-xL	BCL-2	BCL-W	BFL-1	MCL-1	BCL-B
K_D (nM)	0.82	2.04	1.59	16.4	113	146

Fig. 4. Interaction of the newly designed binding site with anti-apoptotic BCL-2 proteins. (A) Schematic indicating the location of mutations introduced into the MCL-1 binding site (triangles) and the BCL-xL binding site (star). (B) Mutations introduced into the BCL-xL binding site. While the I143L substitution is unlikely to disturb BCL-xL binding (left), it is likely to disturb MCL-1 binding by steric hindrance (right). (C) The indicated anti-apoptotic BCL-2 proteins were immobilized on a biosensor chip and their binding affinities were measured via SPR using serially-diluted 4H_αBM_3(I54E/G58E). The K_D values are tabulated. (D) MCL-1 interactions with 4H_αBM_3(L147E/G151E). (*Left*) Schematic indicating the location of mutations introduced into the BCL-xL binding site (triangles). (*Right*) Binding affinity as measured by SPR. 4H_αBM_3(L147E/G151E) was serially diluted and allowed to interact with MCL-1 immobilized on a biosensor chip.

[23,46,47] that facilitates BIM's translocation to the mitochondrial outer membrane, the site of action for the anti-apoptotic BCL-2 proteins. We hypothesized that these two constructs may enhance the apoptogenic efficacy of 4H_αBM_3. The empty vector negative control did not induce cell death in any of the cell lines we tested, nor did expression of αMCL1 or 4H_αBM_3(I54E/G58E), which tar-

get only MCL-1 or BCL-xL, respectively. In contrast, expression of 4H_αBM_3 (targeting both BCL-xL and MCL-1) induced a clear reduction in cell viability (K562: 61%, HCT-116: 79%, SW620: 35%, MEWO: 53%, A375: 22%). Notably, 4H_αBM_3_BH3 and 4H_αBM_3_CTS reduced cell viability even further, confirming that the fused sequences enhance the apoptogenic activity of 4H_αBM_3 (Fig. 5A). We next asked whether the cytotoxic activities observed for these three proteins are stronger than that of full-length human BIM. Although BIM showed strong cytotoxicity, its initial expression level was so high that we had to use 100-fold lower doxycycline concentrations to induce similar levels of protein expression (Fig. 5A, B). After controlling for expression level, we found that 4H_αBM_3, 4H_αBM_3-BH3, and 4H_αBM_3-CTS all exhibit stronger cytotoxicity than human BIM (Fig. 5A, B). Presumably, this higher cytotoxicity reflects the>8-fold higher binding affinity of 4H_αBM_3 than human BIM BH3 [41] for BCL-xL and MCL-1. The cell death we observed was most likely caused by apoptosis, because we confirmed cleavage of the caspase substrate PARP and expression of the cell death marker γ-H2A.X (Fig. 5C).

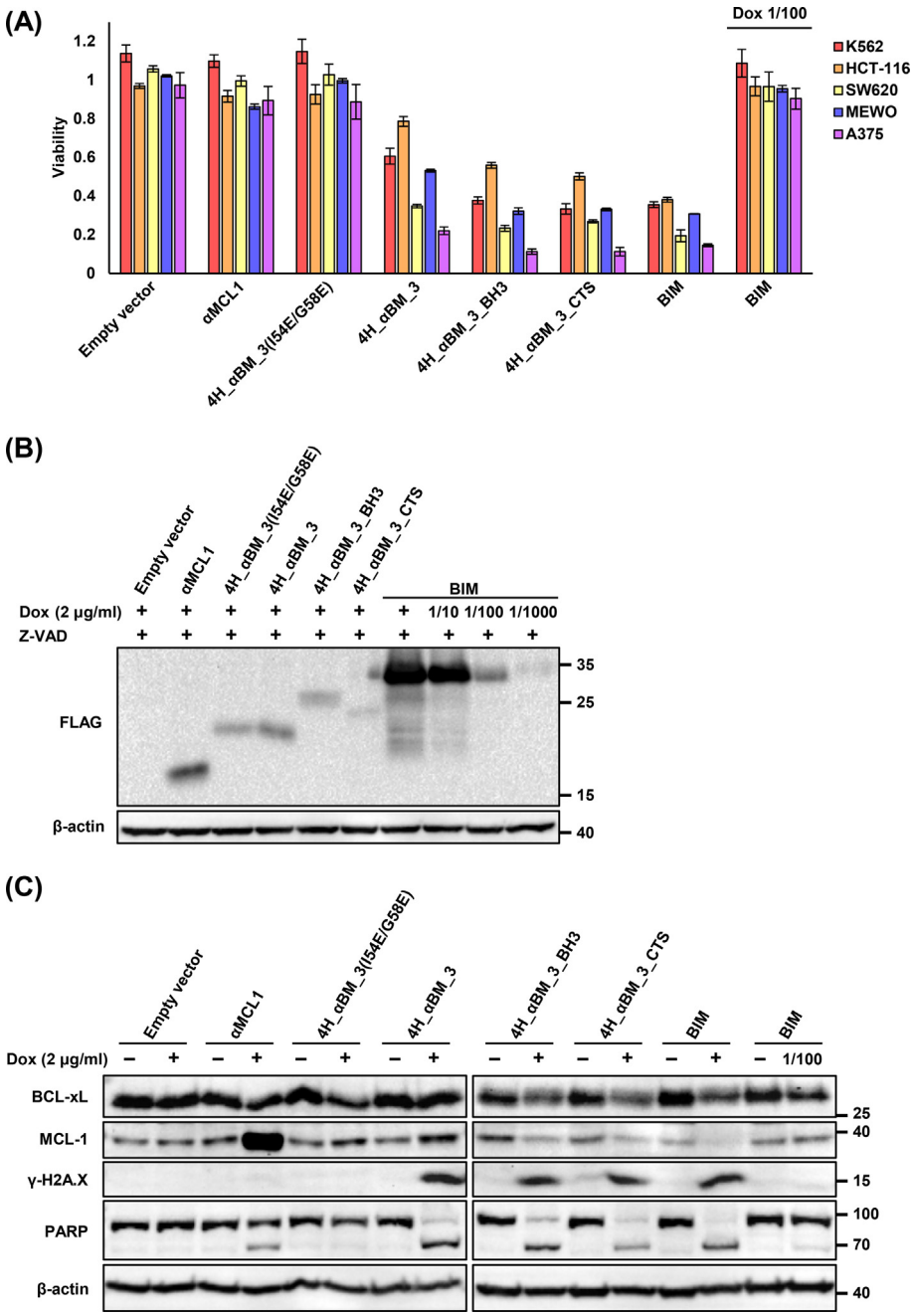

Fig. 5. Cell viability assay. (A) Viability assay. Leukemia (K562), colorectal cancer (HCT-116, SW620), and melanoma (MEWO, A375) cell lines were transduced with lentiviruses that encode each of the indicated constructs with a 3xFLAG tag. Then, cell viability was assayed 12 h after induction by 2 μg/ml doxycycline (Dox) (mean ± SD, n = 3). (B) Doxycycline-induced expression of the indicated proteins in transduced A375 cells as detected by western blotting using an anti-FLAG antibody. Cells were treated with the pan-caspase inhibitor Z-VAD-FMK prior to doxycycline induction to block BIM cleavage. A 10-fold serial dilution of doxycycline from 2 μg/ml was tested to modulate BIM expression. (C) Western blot analysis of transduced A375 cells harvested 12 h after induction by 2 μg/ml doxycycline. The expression of endogenous BCL-xL and MCL-1 along with γ-H2A.X and PARP cleavage were detected.

4. Discussion

Since cancer cells resist apoptosis by upregulating anti-apoptotic BCL-2 proteins [13], the inhibition of BCL-2 proteins should be an effective cancer treatment. Although targeting a single BCL-2 family member has mostly proven ineffective, the simultaneous targeting of two family members produces a synergistic effect [44,45,48,49]. The only exception to this rule appears to be Venetoclax monotherapy, which targets a single anti-apoptotic BCL-2 protein [50]. Several BH3-mimicking small molecules are currently under clinical investigation for use in diverse malignancies as single agents or as components of combination therapies that include either a different BH3 mimetic or a more typical chemotherapeutic drug [51]. Some of these have already shown promise in the treatment of solid tumors and hematological malignancies at the clinical or preclinical stage [51,52]. Since these BH3 mimetics cannot discriminate between normal and cancer cells, their on-target side effects are of primary concern. Many cancers would require targeting multiple anti-apoptotic BCL-2 proteins via BH3 mimetics, especially solid tumors which often exhibit upregulation of multiple BCL-2 family members [53,54]. Such a combination therapy approach, however, would increase the risk of on-target side effects.

Through an iterative computational design and structure determination process, we designed 4H_αBM_3 to bind potently to both BCL-xL and MCL-1, two BCL-2 family members that are often simultaneously upregulated in cancer cells. While 4H_αBM_3 alone triggered apoptotic cell death in five different cancer cells, its fusion to the CTS or BH3 sequences of BIM enhanced its apoptogenic activity. Of the five human cancer cell lines we tested, the A375 melanoma cell was the most susceptible to 4H_αBM_3, but the reasons for this will require further investigation.

For 4H_αBM_3 to be useful as an anti-cancer protein, it must reach the cytoplasm of target cancer cells at a sufficient concentration. In addition, this process must be selective enough for the target cancer cells to avoid on-target side effects. Thus far, targeted intracellular delivery of proteins remains challenging, but it is an area under active investigation [55–60]. On the other hand, the recent success of mRNA vaccines against SARS-CoV-2 has made it practical to deliver therapeutic proteins into the cell cytoplasm in the form of mRNA. The addition of monoclonal antibodies against tumor-associated or tumor-specific antigens to mRNA-encapsulating nanoparticles may make cancer cell-selective expression of encoded therapeutic proteins possible.

4H_αBM_3 may also be useful as a component of a modular protein, maximizing its various endowed activities. For example, 4H_αBM_3 fused to a protein module that engages an E3 ligase could function to remove, rather than inhibit, MCL-1 and BCL-xL. As a proof of concept, we generated 4H_αBM_3-CTS and 4H_αBM_3-BH3 as examples of modular proteins that enhance the activity of 4H_αBM_3. In summary, we have developed a protein that binds potently to both MCL-1 and BCL-xL. We hope to further develop this protein into a clinically relevant anti-cancer therapeutic

Data availability

The coordinates of the structures of 4H_αBM_1-BCL-xL (PDB entry: 7XGG), 4H_αBM_2-BCL-xL (PDB entry: 7XGF),and 4H_αBM_2-MCL-1 (PDB entry: 7XGE) were deposited in the Protein Data Bank.

Author contributions

B.-H.O., H.-S.P., and S.K. conceived this study and wrote the manuscript. S.K. performed the computation and the experiments.

CRediT authorship contribution statement

Seonghoon Kim: Conceptualization, Data curation, Formal analysis, Visualization, Writing - orignal draft, Writing - reviw & editing. **Hee-Sung Park:** Conceptualization, Resources, Writing - review & editing. **Byung-Ha Oh:** Conceptualization, Data curation, Supervision, Funding acquisition, Writing - orignal draft, Writing - reviw & editing.

Declaration of Competing Interests

B.-H.O. and S.K. are co-inventors in a patent application covering the designed proteins described in this article. H.-S.P. declares no competing interests.

Acknowledgments

We thank Dr. Stephanie Berger at Washington University for her insightful suggestions. This study made use of Beamline 5C at Pohang Accelerator Laboratory, South Korea, and was supported by the National Research Foundation of Korea (NRF-2020R1A4A3079755).

References

[1] Suhaili SH, Karimian H, Stellato M, Lee T-H, Aguilar M-I. Mitochondrial outer membrane permeabilization: a focus on the role of mitochondrial membrane structural organization. Biophys Rev 2017;9:443–57. https://doi.org/10.1007/s12551-017-0308-0.
[2] Green DR. The pathophysiology of mitochondrial cell death. Science 2004;305:626–9. https://doi.org/10.1126/science.1099320.
[3] Youle RJ, Strasser A. The BCL-2 protein family: opposing activities that mediate cell death. Nat Rev Mol Cell Biol 2008;9:47–59. https://doi.org/10.1038/nrm2308.
[4] Kale J, Osterlund EJ, Andrews DW. BCL-2 family proteins: changing partners in the dance towards death. Cell Death Differ 2018;25:65–80. https://doi.org/10.1038/cdd.2017.186.
[5] Lovell JF, Billen LP, Bindner S, Shamas-Din A, Fradin C, Leber B, et al. Membrane binding by tBid initiates an ordered series of events culminating in membrane permeabilization by Bax. Cell 2008;135:1074–84. https://doi.org/10.1016/j.cell.2008.11.010.
[6] García-Sáez AJ, Fuertes G, Suckale J, Salgado J. Permeabilization of the Outer Mitochondrial Membrane by Bcl-2 Proteins. Adv Exp Med Biol 2010:91–105. https://doi.org/10.1007/978-1-4419-6327-7_8.
[7] Cosentino K, García-Sáez AJ. Bax and bak pores: are we closing the circle? Trends Cell Biol 2017;27:266–75. https://doi.org/10.1016/j.tcb.2016.11.004.
[8] Shamas-Din A, Kale J, Leber B, Andrews DW. Mechanisms of action of Bcl-2 family proteins. Cold Spring Harb Perspect Biol 2013;5:. https://doi.org/10.1101/cshperspect.a008714a008714.
[9] Leber B, Lin J, Andrews DW. Embedded together: The life and death consequences of interaction of the Bcl-2 family with membranes. Apoptosis 2007;12:897–911. https://doi.org/10.1007/s10495-007-0746-4.
[10] Delbridge ARD, Grabow S, Strasser A, Vaux DL. Thirty years of BCL-2: translating cell death discoveries into novel cancer therapies. Nat Rev Cancer 2016;16:99–109. https://doi.org/10.1038/nrc.2015.17.
[11] Singh R, Letai A, Sarosiek K. Regulation of apoptosis in health and disease: the balancing act of BCL-2 family proteins. Nat Rev Mol Cell Biol 2019;20:175–93. https://doi.org/10.1038/s41580-018-0089-8.
[12] Beroukhim R, Mermel CH, Porter D, Wei G, Raychaudhuri S, Donovan J, et al. The landscape of somatic copy-number alteration across human cancers. Nature 2010;463:899–905. https://doi.org/10.1038/nature08822.
[13] Placzek WJ, Wei J, Kitada S, Zhai D, Reed JC, Pellecchia M. A survey of the anti-apoptotic Bcl-2 subfamily expression in cancer types provides a platform to predict the efficacy of Bcl-2 antagonists in cancer therapy. Cell Death Dis 2010;1:e40.
[14] Punnoose EA, Leverson JD, Peale F, Boghaert ER, Belmont LD, Tan N, et al. Expression profile of BCL-2, BCL-XL, and MCL-1 predicts pharmacological response to the BCL-2 selective antagonist venetoclax in multiple myeloma models. Mol Cancer Ther 2016;15:1132–44. https://doi.org/10.1158/1535-7163.mct-15-0730.
[15] Seiller C, Maiga S, Touzeau C, Bellanger C, Kervoëlen C, Descamps G, et al. Dual targeting of BCL2 and MCL1 rescues myeloma cells resistant to BCL2 and MCL1 inhibitors associated with the formation of BAX/BAK hetero-complexes. Cell Death Dis 2020;11:316. https://doi.org/10.1038/s41419-020-2505-1.
[16] Takahashi H, Chen MC, Pham H, Matsuo Y, Ishiguro H, Reber HA, et al. Simultaneous knock-down of Bcl-xL and Mcl-1 induces apoptosis through Bax activation in pancreatic cancer cells. Biochim Biophys Acta 2013;1833:2980–7. https://doi.org/10.1016/j.bbamcr.2013.08.006.

[17] Varin E, Denoyelle C, Brotin E, Meryet-Figuière M, Giffard F, Abeilard E, et al. Downregulation of Bcl-x L and Mcl-1 is sufficient to induce cell death in mesothelioma cells highly refractory to conventional chemotherapy. Carcinogenesis 2010;31:984–93. https://doi.org/10.1093/carcin/bgq026.
[18] Kotschy A, Szlavik Z, Murray J, Davidson J, Maragno AL, Le Toumelin-Braizat G, et al. The MCL1 inhibitor S63845 is tolerable and effective in diverse cancer models. Nature 2016;538:477–82. https://doi.org/10.1038/nature19830.
[19] Yasuda Y, Ozasa H, Kim YH, Yamazoe M, Ajimizu H, Funazo TY, et al. MCL1 inhibition is effective against a subset of small-cell lung cancer with high MCL1 and low BCL-XL expression. Cell Death Dis 2020;11. https://doi.org/10.1038/s41419-020-2379-2.
[20] Moujalled DM, Pomilio G, Ghiurau C, Ivey A, Salmon J, Rijal S, et al. Combining BH3-mimetics to target both BCL-2 and MCL1 has potent activity in pre-clinical models of acute myeloid leukemia. Leukemia 2019;33:905–17. https://doi.org/10.1038/s41375-018-0261-3.
[21] Walensky LD, Kung AL, Escher I, Malia TJ, Barbuto S, Wright RD, et al. Activation of apoptosis in vivo by a hydrocarbon-stapled BH3 helix. Science 2004;305:1466–70. https://doi.org/10.1126/science.1099191.
[22] Sarosiek KA, Fraser C, Muthalagu N, Bhola PD, Chang W, McBrayer SK, et al. Developmental regulation of mitochondrial apoptosis by c-myc governs age- and tissue-specific sensitivity to cancer therapeutics. Cancer Cell 2017;31:142–56. https://doi.org/10.1016/j.ccell.2016.11.011.
[23] Walensky LD, Pitter K, Morash J, Oh KJ, Barbuto S, Fisher J, et al. A stapled BID BH3 helix directly binds and activates BAX. Mol Cell 2006;24:199–210. https://doi.org/10.1016/j.molcel.2006.08.020.
[24] Steele TM, Talbott GC, Sam A, Tepper CG, Ghosh PM, Vinall RL. Obatoclax a BH3 mimetic, enhances cisplatin-induced apoptosis and decreases the clonogenicity of muscle invasive bladder cancer cells via mechanisms that involve the inhibition of pro-survival molecules as well as cell cycle regulators. Int J Mol Sci 2019;20. https://doi.org/10.3390/ijms20061285.
[25] Merino D, Kelly GL, Lessene G, Wei AH, Roberts AW, Strasser A. BH3-mimetic drugs: blazing the trail for new cancer medicines. Cancer Cell 2018;34:879–91. https://doi.org/10.1016/j.ccell.2018.11.004.
[26] Adams CM, Clark-Garvey S, Porcu P, Eischen CM. Targeting the Bcl-2 family in B cell lymphoma. Front Oncol 2019;8. https://doi.org/10.3389/fonc.2018.00636.
[27] Procko E, Berguig GY, Shen BW, Song Y, Frayo S, Convertine AJ, et al. A computationally designed inhibitor of an Epstein-Barr viral Bcl-2 protein induces apoptosis in infected cells. Cell 2014;157:1644–56. https://doi.org/10.1016/j.cell.2014.04.034.
[28] Berger S, Procko E, Margineantu D, Lee EF, Shen BW, Zelter A, et al. Computationally designed high specificity inhibitors delineate the roles of BCL2 family proteins in cancer. Elife 2016;5. https://doi.org/10.7554/eLife.20352.
[29] Leman JK, Weitzner BD, Lewis SM, Adolf-Bryfogle J, Alam N, Alford RF, et al. Macromolecular modeling and design in Rosetta: recent methods and frameworks. Nat Methods 2020;17:665–80. https://doi.org/10.1038/s41592-020-0848-2.
[30] Huang P-S, Oberdorfer G, Xu C, Pei XY, Nannenga BL, Rogers JM, et al. High thermodynamic stability of parametrically designed helical bundles. Science 2014;346:481–5. https://doi.org/10.1126/science.1257481.
[31] Huang P-S, Ban Y-EA, Richter F, Andre I, Vernon R, Schief WR, et al. RosettaRemodel: a generalized framework for flexible backbone protein design. PLoS One 2011;6:e24109. https://doi.org/10.1371/journal.pone.0024109.
[32] Bhardwaj G, Mulligan VK, Bahl CD, Gilmore JM, Harvey PJ, Cheneval O, et al. Accurate de novo design of hyperstable constrained peptides. Nature 2016;538:329–35. https://doi.org/10.1038/nature19791.
[33] Fleishman SJ, Leaver-Fay A, Corn JE, Strauch E-M, Khare SD, Koga N, et al. RosettaScripts: a scripting language interface to the Rosetta macromolecular modeling suite. PLoS ONE 2011;6:e20161.
[34] Lee EF, Sadowsky JD, Smith BJ, Czabotar PE, Peterson-Kaufman KJ, Colman PM, et al. High-resolution structural characterization of a helical alpha/beta-peptide foldamer bound to the anti-apoptotic protein Bcl-xL. Angew Chem Int Ed Engl 2009;48:4318–22. https://doi.org/10.1002/anie.200805761.
[35] Afonine PV, Grosse-Kunstleve RW, Echols N, Headd JJ, Moriarty NW, Mustyakimov M, et al. Towards automated crystallographic structure refinement with phenix.refine. Acta Crystallogr D Biol Crystallogr 2012;68:352–67. https://doi.org/10.1107/S0907444912001308.
[36] McCoy AJ, Grosse-Kunstleve RW, Adams PD, Winn MD, Storoni LC, Read RJ. Phaser crystallographic software. J Appl Crystallogr 2007;40:658–74. https://doi.org/10.1107/S0021889807021206.
[37] Emsley P, Lohkamp B, Scott WG, Cowtan K. Features and development of Coot. Acta Crystallogr D Biol Crystallogr 2010;66:486–501. https://doi.org/10.1107/S0907444910007493.
[38] Pymol DWL. An open-source molecular graphics tool. CCP4 Newsl Protein Crystallogr 2002.
[39] Chipuk JE, Moldoveanu T, Llambi F, Parsons MJ, Green DR. The BCL-2 family reunion. Mol Cell 2010;37:299–310. https://doi.org/10.1016/j.molcel.2010.01.025.
[40] Rajan S, Choi M, Baek K, Yoon HS. Bh3 induced conformational changes in Bcl-Xl revealed by crystal structure and comparative analysis. Proteins 2015;83:1262–72. https://doi.org/10.1002/prot.24816.
[41] Ku B, Liang C, Jung JU, Oh B-H. Evidence that inhibition of BAX activation by BCL-2 involves its tight and preferential interaction with the BH3 domain of BAX. Cell Res 2011;21:627–41. https://doi.org/10.1038/cr.2010.149.
[42] Willis SN, Fletcher JI, Kaufmann T, van Delft MF, Chen L, Czabotar PE, et al. Apoptosis initiated when BH3 ligands engage multiple Bcl-2 homologs, not Bax or Bak. Science 2007;315:856–9. https://doi.org/10.1126/science.1133289.
[43] Polster BM, Kinnally KW, Fiskum G. BH3 death domain peptide induces cell type-selective mitochondrial outer membrane permeability. J Biol Chem 2001;276:37887–94. https://doi.org/10.1074/jbc.M104552200.
[44] Lee EF, Harris TJ, Tran S, Evangelista M, Arulananda S, John T, et al. BCL-XL and MCL-1 are the key BCL-2 family proteins in melanoma cell survival. Cell Death Dis 2019;10:342. https://doi.org/10.1038/s41419-019-1568-3.
[45] Okumura K, Huang S, Sinicrope FA. Induction of Noxa sensitizes human colorectal cancer cells expressing Mcl-1 to the small-molecule Bcl-2/Bcl-xL inhibitor, ABT-737. Clin Cancer Res 2008;14:8132–42. https://doi.org/10.1158/1078-0432.CCR-08-1665.
[46] Liu Q, Osterlund EJ, Chi X, Pogmore J, Leber B, Andrews DW. Bim escapes displacement by BH3-mimetic anti-cancer drugs by double-bolt locking both Bcl-XL and Bcl-2. Elife 2019;8. https://doi.org/10.7554/eLife.37689.
[47] Chi X, Nguyen D, Pemberton JM, Osterlund EJ, Liu Q, Brahmbhatt H, et al. The carboxyl-terminal sequence of bim enables bax activation and killing of unprimed cells. Elife 2020;9. https://doi.org/10.7554/eLife.44525.
[48] Weeden CE, Ah-Cann C, Holik AZ, Pasquet J, Garnier J-M, Merino D, et al. Dual inhibition of BCL-XL and MCL-1 is required to induce tumour regression in lung squamous cell carcinomas sensitive to FGFR inhibition. Oncogene 2018;37:4475–88. https://doi.org/10.1038/s41388-018-0268-2.
[49] Cao X, Yap JL, Newell-Rogers MK, Peddaboina C, Jiang W, Papaconstantinou HT, et al. The novel BH3 α-helix mimetic JY-1-106 induces apoptosis in a subset of cancer cells (lung cancer, colon cancer and mesothelioma) by disrupting Bcl-xL and Mcl-1 protein–protein interactions with Bak. Mol Cancer 2013;12:42. https://doi.org/10.1186/1476-4598-12-42.
[50] Souers AJ, Leverson JD, Boghaert ER, Ackler SL, Catron ND, Chen J, et al. ABT-199, a potent and selective BCL-2 inhibitor, achieves antitumor activity while sparing platelets. Nat Med 2013;19:202–8. https://doi.org/10.1038/nm.3048.
[51] Cerella C, Dicato M, Diederich M. BH3 mimetics in AML therapy: death and beyond? Trends Pharmacol Sci 2020;41:793–814. https://doi.org/10.1016/j.tips.2020.09.004.
[52] Carter RJ, Milani M, Butterworth M, Alotibi A, Harper N, Yedida G, et al. Exploring the potential of BH3 mimetic therapy in squamous cell carcinoma of the head and neck. Cell Death Dis 2019;10:912. https://doi.org/10.1038/s41419-019-2150-8.
[53] Caenepeel S, Brown SP, Belmontes B, Moody G, Keegan KS, Chui D, et al. AMG 176, a Selective MCL1 Inhibitor, is Effective in Hematological Cancer Models Alone and in Combination with Established Therapies. Cancer Discovery 2018: CD – 18. https://doi.org/10.1158/2159-8290.cd-18-0387.
[54] Ramsey HE, Fischer MA, Lee T, Gorska AE, Arrate MP, Fuller L, et al. A novel MCL1 inhibitor combined with venetoclax rescues venetoclax-resistant acute myelogenous leukemia. Cancer Discovery 2018;8:1566–81. https://doi.org/10.1158/2159-8290.cd-18-0140.
[55] Choi H, Choi Y, Yim HY, Mirzaaghasi A, Yoo J-K, Choi C. Biodistribution of exosomes and engineering strategies for targeted delivery of therapeutic exosomes. Tissue Eng Regen Med 2021;18:499–511. https://doi.org/10.1007/s13770-021-00361-0.
[56] Huda MN, Nafiujjaman M, Deaguero IG, Okonkwo J, Hill ML, Kim T, et al. Potential use of exosomes as diagnostic biomarkers and in targeted drug delivery: progress in clinical and preclinical applications. ACS Biomater Sci Eng 2021;7:2106–49. https://doi.org/10.1021/acsbiomaterials.1c00217.
[57] Sánchez-Navarro M. Advances in peptide-mediated cytosolic delivery of proteins. Adv Drug Deliv Rev 2021;171:187–98. https://doi.org/10.1016/j.addr.2021.02.003.
[58] Zhang S, Shen J, Li D, Cheng Y. Strategies in the delivery of Cas9 ribonucleoprotein for CRISPR/Cas9 genome editing. Theranostics 2021;11:614–48. https://doi.org/10.7150/thno.47007.
[59] Heimann AS, Dale CS, Guimarães FS, Reis RAM, Navon A, Shmuelov MA, et al. Hemopressin as a breakthrough for the cannabinoid field. Neuropharmacology 2021;183:. https://doi.org/10.1016/j.neuropharm.2020.108406108406.
[60] Rosenkranz AA, Slastnikova TA. Epidermal growth factor receptor: key to selective intracellular delivery. Biochemistry 2020;85:967–1092. https://doi.org/10.1134/S0006297920090011.